Plasmonic Cu$_{27}$S$_{24}$ nanocages for novel solar photothermal nanoink and nanofilm

Min Xi[1,2,§] (✉), Longchang Xu[1,3,§], Nian Li[1], Shudong Zhang[1] (✉), and Zhenyang Wang[1] (✉)

[1] Institute of Solid State Physics and Key Laboratory of Photovoltaic and Energy Conservation Materials, Hefei Institutes of Physical Science, Chinese Academy of Sciences, Hefei 230031, China
[2] The Key Laboratory Functional Molecular Solids Ministry of Education, Anhui Normal University, Wuhu 241002, China
[3] School of Mechatronics and Vehicle Engineering, Chongqing Jiaotong University, Chongqing 400074, China
[§] Min Xi and Longchang Xu contributed equally to this work.

ABSTRACT

Copper sulfide (Cu$_x$S) as a plasmonic solar photothermal semiconductor material that expands the light collection range by altering localized surface plasmon resonance (LSPR) to the near- to mid- infrared (IR) spectral region. The versatile synthesis strategies of Cu$_x$S nanostructure offer its variability of morphology and provide additional freedom in tuning the optical property. Particularly, nanocage (or nanoshell) has hybridized plasmon resonances as a result of super-positioned nanosphere and nanocavity, which extends its receiving range of solar spectrum and increases light-to-heat conversion rate. Here, we offer novel "nanoink" and "nanofilm" developed from colloidal Cu$_{27}$S$_{24}$ nanocages with excellent solar photothermal response. Via combining experimental measurement and theoretical calculation, we estimated the optical properties of covellite Cu$_{27}$S$_{24}$. And based on obtained dielectric functions, we then calculated its solar photothermal performance, which was further validated by our experimental measurement. The simulation results showed that hollow Cu$_{27}$S$_{24}$ nanocages have excellent solar photothermal performance, and exhibit much higher solar photothermal conversion efficiency than solid Cu$_{27}$S$_{24}$ nanospheres.

KEYWORDS

plasmonics, solar photothermal, hybridized plasmon, Cu$_{27}$S$_{24}$ nanocages

1   Introduction

Plasmonic materials exhibit superior light-to-heat conversion efficiency [1–3]. As a unique optical phenomenon of micro/nanostructure, the localized surface plasmon resonance (LSPR) effect of metal nanoparticles can be described by the Drude free electron model [4, 5]. When the incident light triggers the plasmonic resonance of the metal structure of subwavelength dimension, the oscillation of the free electrons will raise the temperature of metal surface and surrounding via intense electron-electron and electron-phonon interactions [6–8].

Compare to traditional noble metals such as silver and gold that have LSPR in the ultraviolet-visible (UV–vis) range, semiconductors exhibit LSPR in the near- to mid- infrared (IR) spectral region, which expands the light collection range [9–12]. The nanostructure of semiconducting material can tune its LSPR by adjusting its optical property in terms of its carrier concentration, which can be realized by introducing atoms of impurities (doping) or altering the composition of compound into non-stoichiometry [13]. For example, dielectric function of indium (III) oxide can be tuned by incorporating tin (IV) atoms, which leads to its tunable LSPR from ~ 3,200 nm with 1.5% doping to ~ 1,400 nm with ~ 10% doping [14]. In addition to that, similar to conventional noble metal nanostructure, semiconducting nanostructure also shows its LSPR tunability by adjusting its morphology [15, 16]. For example, Martina et al.

deposited metal oxides nanorods arrays on CaF$_2$ windows. And the plasmonic nanoantenna showed tunable resonance from 3 to 10 μm by varying the array spacing and aspect ratio of antenna, which can be used for extraordinary sensitivity for infrared molecular signals [17].

Semiconductor copper sulfide copper sulfide (Cu$_x$S) of non-stoichiometry has been studied extensively for its plasmonic effect in the infrared range [16, 18]. Numerous theoretical and experimental studies have proven that Cu$_x$S exists in different stable formations from copper rich chalcocite (Cu$_2$S), to analite non-stoichiometric (Cu$_7$S$_4$), and sulfur rich covellite (CuS) phases [16, 19–21]. Their different crystallizations provide unique properties (such as band gap, bond length, oxidation state of atoms, etc.) in a vast range, such as: electronic or photocatalyst [22, 23], solar cells [19], biosensors [24], drug delivery [21], crystal liquids [16], etc. Despite the availability and stability of Cu$_x$S, versatile synthesis strategies offer its variability of morphology as well as additional freedom in tuning the optical property. For example, CuS quantum dot (QD) shows LSPR in the near-IR (~ 1,000 nm) [24], while CuS nanoplate has the LSPR at ~ 1,200 nm [25]. Particularly, the small bandgap and wide peak width grant its high solar photothermal conversion efficiency, especially the high utilization of energy in the IR range [26, 27].

Particularly, plasmon resonances of hollow nanocage (or nanoshell) can be regarded as the hybridized "bonding" and "antibonding" mode plasmons of super-positioned nanosphere

---

and nanocavity [28]. The splitted resonances offer extraordinary photothermal performance by enlarging light collecting range and decreasing radiation dissipation energy [28–30], which can be applied in a vast of areas, such as biomarking [31], photothermal therapy [32], etc.

In this paper, we introduce novel "nanoink" and "nanofilm" with excellent photothermal performance developed from colloidal $Cu_{27}S_{24}$ nanocages. Firstly, the $Cu_{27}S_{24}$ nanocages were successfully synthesized, and developed into "nanoink" with extraordinary photothermal response. Then we use theoretical approach by combining first-principle calculations and electromagnetic numerical simulations to approximate the optical property of $Cu_{27}S_{24}$. Based on this estimated dielectric function of $Cu_{27}S_{24}$, we calculated the solar photothermal behavior of $Cu_{27}S_{24}$ nanocage/polyvinylidene fluoride (PVDF) "nanofilm", which exhibited extraordinary light-to-heat conversion efficiency, and corroborated by solar photothermal measurement. Our further simulation results showed that the hollow $Cu_{27}S_{24}$ nanocages have much higher photothermal conversion efficiency than solid $Cu_{27}S_{24}$ nanospheres. And the $Cu_{27}S_{24}$ nanocages with different shell thickness are also evaluated and discussed.

2   Results and discussion

Cu_xS nanocages were prepared according to the literature reference (see Methods for synthesis details). Basically, the hollow Cu_xS nanocages were synthesized via hydrothermal chemical conversion from Cu_2O nanospheres (Fig. 1(a)).

The synthesized nanoparticles were examined with field emission scanning electron microscope (FE-SEM, Sirion200) and transmission electron microscopy (TEM, Hitachi H-9000 NAR instrument) for morphological characterization. Figures 1(b) and 1(c) and Figs. 1(d) and 1(e) show the typical scanning electron microscope (SEM) and TEM images of hollow nanocages. The dark edges and transparent central region prove the hollow shape of nanocage, which reveals the hollow hierarchical micro-/nano-structures. The statistical count of nanostructure sizes are summarized in Figs. S1(a) and S1(b) in the Electronic Supplementary Material (ESM) after the images processed by Nano Measure software (see Methods for details). The average diameter and shell thickness of nanocage are estimated as 150 and 20 nm, respectively.

Then we study the optical property of Cu_xS nanocage, which depends on both the geometry of nanoparticle and dielectric function of Cu_xS. We calculated the dielectric function of Cu_xS by comparing simulated spectrum to experimental measured spectrum. Since Mie theory can only be applied to spherical shaped nanoparticle, we performed numerical electromagnetic simulations to calculate the spectrum of Cu_xS nanocages with derived dielectric function from first-principle calculation.

The first-principle calculation was performed using the CASTEP module of materials studio. Since the atom percentage ratio between copper and sulphur is close to 9:8 determined by the energy dispersive spectroscopy (EDS) elemental analysis results shown in Fig. S2 in the ESM. And the phase and purity of the products were determined by X-ray powder diffraction (PXRD) using an X-ray diffractometer with Cu Kα radiation ($\lambda = 1.5418$ Å). Scans were collected on dry powder in the range of 10°–80°. The XRD spectra of the sample in Fig. S3 in the ESM indicates the obtained copper sulfide matches the card of JSPD-06–0464, and can be indexed well to the phase of covellite. Therefore, the supercell lattice structure was built with the parameters of Cu_xS adopted from reported lattice structure of covellite [33], and then corrected into $Cu_{27}S_{24}$ to optimize the atom ratio. The lattice structure was first performed with geometry optimization and then the optical properties were calculated.

The optimized supercell lattice is shown in Fig. 2(a), and the corresponding atom coordinates are shown in Table S1 in the ESM. In the optimized supercell, there are multiple types of hybridized copper atom attached to different number of adjacent atoms due to the defects of non-stoichiometric atom ratio, which is further corroborated by Fourier transform infrared (FTIR) measurement results. The Cu–S stretching modes vibrational
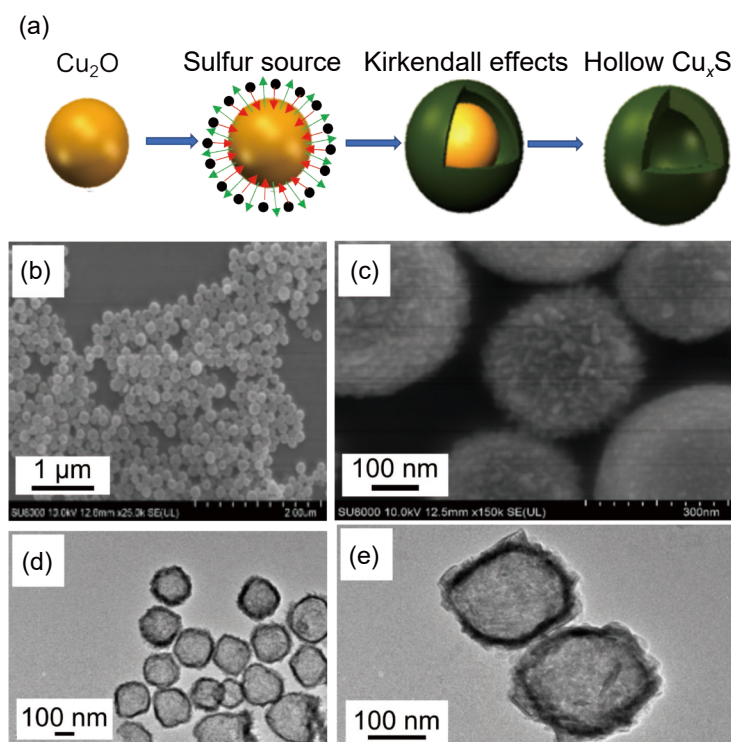
Figure 1   (a) Scheme illustrates the Kirkendall effects in the formation of Cu_xS nanocages; (b) and (c) low and high magnification SEM images of hollow Cu_xS nanocages; (d) and (e) low and high magnification TEM images of Cu_xS nanocages.
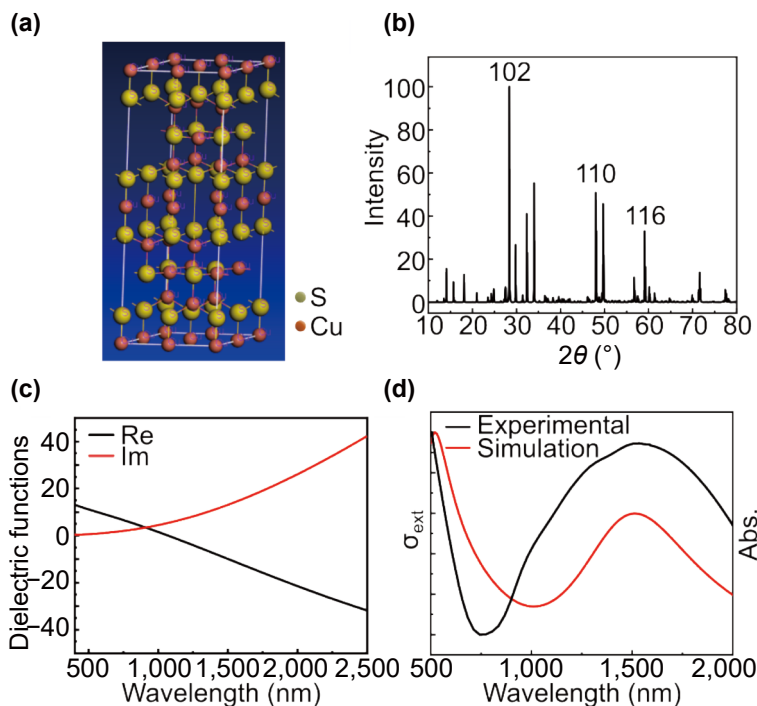
Figure 2 (a) Lattice structure of modeled $Cu_{27}S_{24}$ supercell; (b) calculated XRD pattern of modeled $Cu_{27}S_{24}$ supercell; (c) calculated dielectric function of $Cu_{27}S_{24}$ in complex form of both real (black line) and imaginary (red line); (d) simulated and normalized extinction cross section (red line) and experimental measured UV–vis-NIR spectra (black line) of $Cu_{27}S_{24}$ nanocages.

peaks at 620 cm^{-1} shown in Fig. S4 in the ESM [34], and its adjacent multiple bands suggest the co-existence of different covalent Cu–S bonds.

The number ratio between copper atoms attached to 4 adjacent atoms and that attached to 2 adjacent atoms is 1.70, which matches the X-ray photoelectron spectroscopy (XPS) characterization results in Figs. S5(a) and S5(b) in the ESM. The binding energy peaks can be assigned to atoms oxidation states of Cu 2p$_{3/2}$ (951.5 eV), Cu 2p$_{1/2}$ (931.7 eV) and S 2p$_{3/2}$ (162.8 eV), S 2p$_{1/2}$ (161.8 eV) [35], and the peak energy ratio between Cu 2p$_{3/2}$ (951.5 eV) and Cu 2p$_{1/2}$ (931.7 eV) is 1.66. The peak intensity ratio between S 2p$_{3/2}$ and S 2p$_{1/2}$ is ~ 1.30, which contributes to alternating S$_2$ and CuS$_3$-CuS$_3$ layers arranged by monosulfides (S^{2-}) and disulfides (S^{1-}-S^{1-}) S atoms. This formation preferably exists in stable CuS of covellite rather than Cu$_2$S of chalcocite at ambient condition [20].

The calculated X-ray diffraction (XRD) pattern is shown in Fig. 2(b), whose characteristic peaks at 28.3°, 48.1° and 59.1° correspond to the measured XRD pattern peaks of 29.6°, 48.4° and 60.0° in Fig. S3 in the ESM should be assigned to the (102), (110) and (116) planes of covellite lattice, which further confirms the validity of our modeled supercell lattice structure, since the Cu$_x$S with stoichiometry close to 1 shows rich covellite lattice [26].

The complex dielectric function $\varepsilon_{re} + i\varepsilon_{im}$ of Cu$_{27}$S$_{24}$ was then calculated by CASTEP module. Basically, the $\gamma = 0.44$ eV and different values of bulk plasma frequency ω_p were used to estimate the dielectric function according to the literature reference (Fig. S6(a) in the ESM) [25]. We performed numerical simulations of hollow Cu$_{27}$S$_{24}$ nanocages (Fig. S6(b) in the ESM) with each derived dielectric function of Cu$_{27}$S$_{24}$ to select the most accurate one by comparing the simulated spectrum to experimental value (Figs. S6(c) and S6(d) in the ESM). The bulk plasma frequencies of the synthesized Cu$_{27}$S$_{24}$ material can be calculated from the semi-empirical equation, and $\omega_p = 4.30$ eV was used to derive the resulting dielectric function of Cu$_{27}$S$_{24}$. The estimated dielectric functions are plotted in Fig. 2(c), and the derived carrier concentration $n_e = 5.40 \times 10^{21}$ cm^{-3} agrees with the reported value [18].

The simulated spectrum is shown in Fig. 2(d) as red line, which is comparable to the experimental measured UV–vis-NIR spectra (black line), though the full width at half maximum (FWHM) of the simulation (0.31 eV) is smaller than the experimental value of 1.27 eV due to the anisotropic broadening caused by large size and shape distribution of the synthesized nanoparticles.

The synthesized Cu$_{27}$S$_{24}$ nanocages can be well dispersed in aqueous phase as "nanoink" (Fig. 3(a)). The Tyndall effect of above "nanoink" indicates highly monodispersed and stable colloidal nanocages in ethanol. The "nanoink" can be directly written on dark paper into designed pattern via calligraphy paint brush (Fig. 3(b)), and the written words became almost indiscernible for naked eyes after ethanol solvent being evaporated completely (Fig. 3(c)). Interesting, the written pattern can be revealed with IR camera when the calligraphy was placed under solar irradiance (Fig. 3(d)). This remarkable phenomenon proves the extraordinary photothermal response of pattern regions that lead to the high temperature exceeds other carbon ink regions of the native dark color paper.

In order to statistically study the photothermal performance of Cu$_{27}$S$_{24}$ nanocages, we made a series of Cu$_{27}$S$_{24}$ nanocage/polyvinylidene fluoride nanofilms (please refer to Methods for details). Typically, the Cu$_{27}$S$_{24}$ nanocage/PVDF nanofilm was fabricated via evaporating the mixture of colloidal Cu$_{27}$S$_{24}$ nanocages dispersed in PVDF and N,N-dimethylformamide (DMF) mixed solution. As shown in Fig. 3(e), as the Cu$_{27}$S$_{24}$ nanocage loading amount increases, the color of film gets darker. The photothermal test was performed by placing the Cu$_{27}$S$_{24}$ nanocage/PVDF film under solar irradiance, and the film temperature was recorded as by IR camera. The curves in Fig. 3(f) show that the film temperature increased and reached a plateau of equilibrium after ~ 5 min illumination. And the temperature at equilibrium increases as the Cu$_{27}$S$_{24}$ nanocage loading weight. We simulated photothermal response of the film with heat transfer module of COMSOL multiphysics (see Methods and Fig. S7 in the ESM for simulation details). The simulated results are plotted in Fig. 3(g), which basically follow the trends of experimental results. The temperature curves at
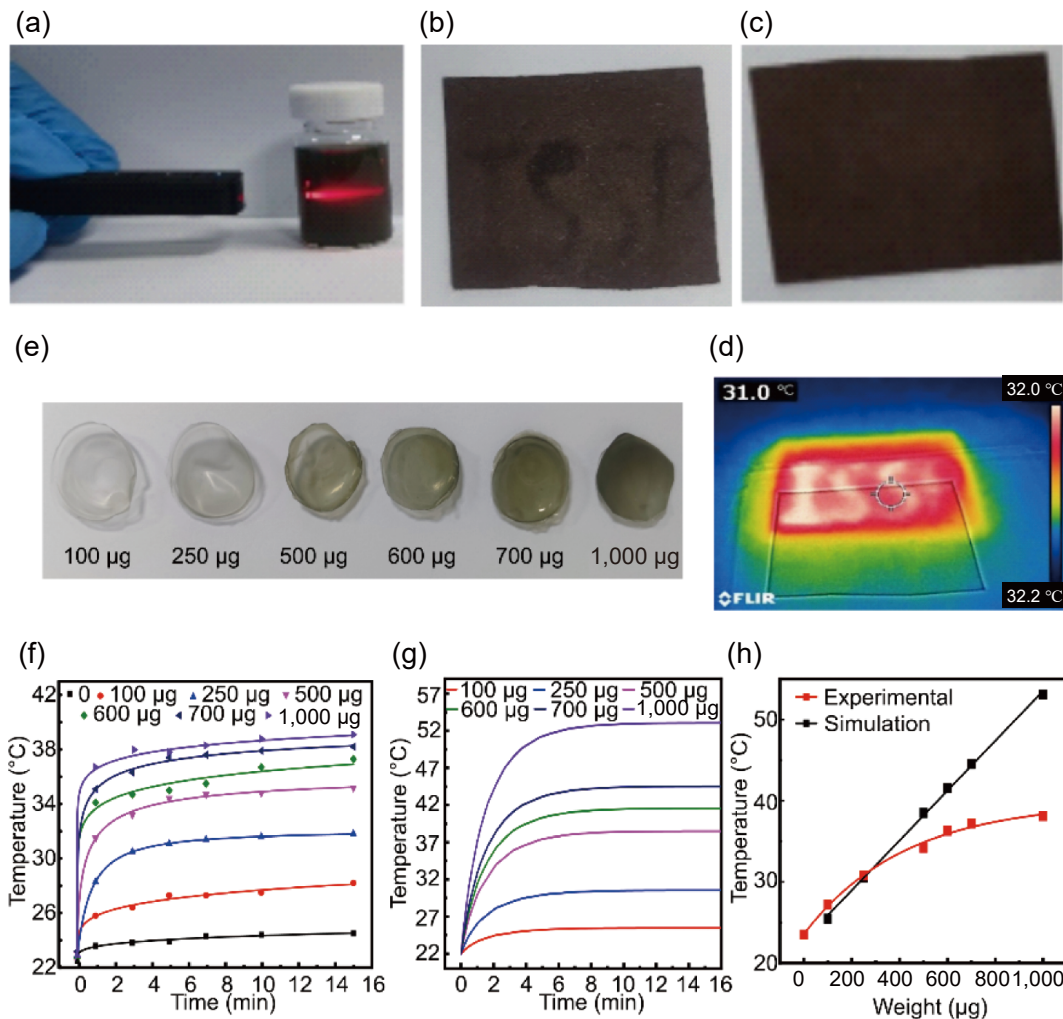
Figure 3 (a) Photograph of $Cu_{27}S_{24}$ nanocage ink with Tyndall effects; (b) and (c) photograph of $Cu_{27}S_{24}$ nanoink on dark paper before and after solvent evaporation; (d) photothermal performance of $Cu_{27}S_{24}$ nanoink on dark paper; (e) the photograph of $Cu_{27}S_{24}$ nanocage/PVDF nanofilms with different loading of $Cu_{27}S_{24}$ nanocages; (f) and (g) experimental measured and simulated photothermal performance of $Cu_{27}S_{24}$ nanocage/PVDF nanofilm with different $Cu_{27}S_{24}$ loading weights; (h) equilibrium temperature of $Cu_{27}S_{24}$ nanocage/PVDF nanofilm with different $Cu_{27}S_{24}$ loading weight.

equilibrium of $Cu_{27}S_{24}$ nanocage/PVDF nanofilm with different $Cu_{27}S_{24}$ nanocage loading weights are summarized in Fig. 3(h). Both simulated and experimental curves showed that the equilibrium temperature increased with loading weight in the nanofilm. It should be noticed that the experimental curves have lower slope than the simulated one, which may be contributed by the underestimation of heat dissipation loss due to the simulation boundary condition and heat transfer coefficient.

The photothermal conversion efficiency of these nanofilms were calculated. The energy conversion efficiency was calculated as: $\eta = \dfrac{C_p m_{film} \Delta T}{P S_A t}$, where C_p and m_{film} are the heat capacitance (2,500 J/(kg·K)) and mass of the film (~ 0.2 g), ΔT is the temperature change, and P is the solar irradiance power (~ 1,000 W/m²), S_A is the area of the nanofilm (~ 3 cm²), and we choose illumination time $t = 3$ min before nanofilm reaching the temperature of equilibrium for calculation. Summarized in Table S2 in the ESM, the experimental value of photothermal conversion efficiency increased from 1.2% with $Cu_{27}S_{24}$ nanoscages loading weight of 100 μg to 11.6% with 1,000 μg $Cu_{27}S_{24}$ nanoscages, which generally follow the trend of the simulated value from 2.5% to 22.9%.

In addition, we compared the photothermal performance of solid $Cu_{27}S_{24}$ nanocage/PVDF and $Cu_{27}S_{24}$ nanosphere/PVDF nanofilm. Shown in Fig. 4(a), we modeled solid $Cu_{27}S_{24}$

nanosphere of the same size (outer diameter of 150 nm) to hollow $Cu_{27}S_{24}$ nanocage. Indicated in Fig. 4(b) as green curve, the calculated spectrum of solid $Cu_{27}S_{24}$ nanosphere (diameter of 150 nm) is slightly blue shifted and shows stronger peak intensity compared to hollow $Cu_{27}S_{24}$ nanocage (blue curve). Based on these calculated optical properties of solid nanosphere and hollow nanocages, we then used heat transfer module to simulate photothermal performance of $Cu_{27}S_{24}$ nanosphere/PVDF nanofilm and $Cu_{27}S_{24}$ nanocage/PVDF nanofilm.

The photothermal simulation with similar setup mentioned above was performed, and the simulated photothermal response of each film and temperature at equilibrium are summarized in Figs. 4(c) and 4(d). Similar to $Cu_{27}S_{24}$ nanocage/PVDF nanofilm (Figs. 3(g) and 3(h)), both the temperature rising rate and equilibrium temperature of nanofilm increase as the loading weight of $Cu_{27}S_{24}$ nanosphere in the film.

To the best of our knowledge, the method to synthesize solid Cu_xS nanosphere to the similar size of $Cu_{27}S_{24}$ nanocage (~ 150 nm) has not been reported yet. Alternatively, we synthesized Cu_xS nanodisks, and converted them into agglomerated Cu_xS nanodisk clusters by dispersing them in the mixed solution of ethanol and cyclohexane (see Methods for experimental details) [36]. And the desired size of ~ 150 nm was obtained by fractional centrifugation and measured by dynamic light scattering (see Fig. S8 in the ESM for differential locj system
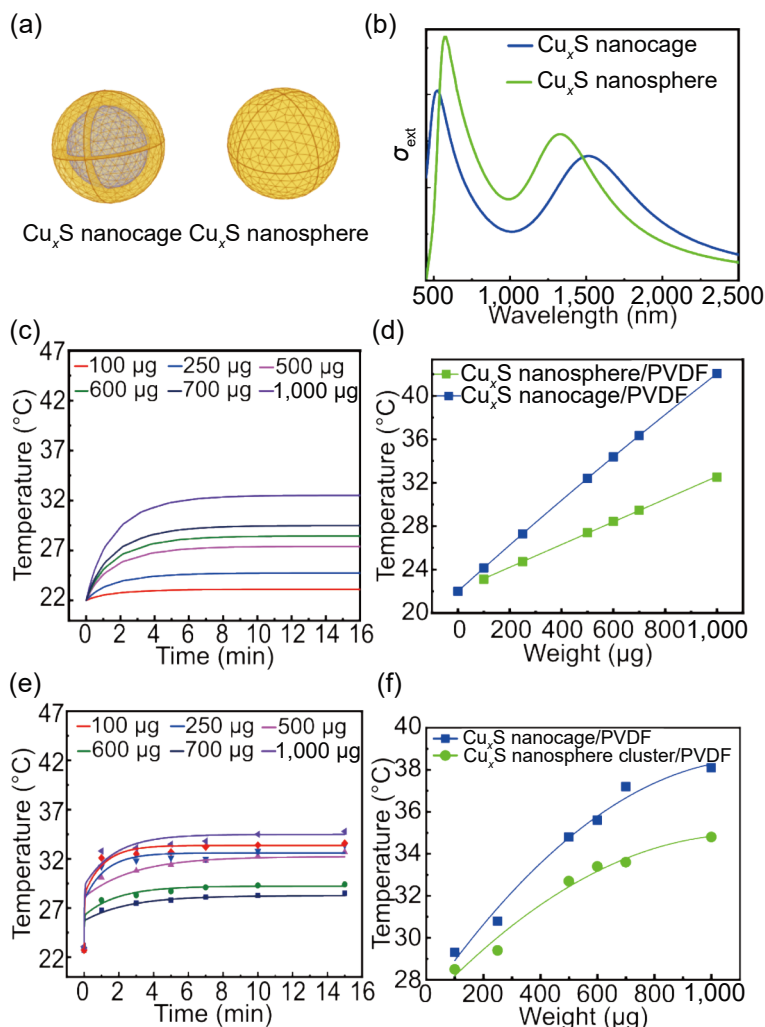
Figure 4 (a) Scheme show hollow nanocage and solid nanosphere of same size; (b) simulated extinction cross section of $Cu_{27}S_{24}$ nanocage (blue line) and $Cu_{27}S_{24}$ nanosphere (green line); (c) simulated photothermal performance of $Cu_{27}S_{24}$ nanosphere/PVDF nanofilm with different $Cu_{27}S_{24}$ nanosphere loading weights; (d) simulated equilibrium temperature of $Cu_{27}S_{24}$ nanocage/PVDF nanofilm (blue line) and $Cu_{27}S_{24}$ nanosphere/PVDF nanofilm (green line) with different loading weights; (e) experimental measured photothermal performance of Cu_xS nanodisk cluster/PVDF nanofilm with different Cu_xS nanodisk cluster loading weights; (f) experimental measured equilibrium temperature of $Cu_{27}S_{24}$ nanocage/PVDF nanofilm (blue line) and Cu_xS nanodisk cluster/PVDF nanofilm (green line) with different Cu_xS nanodisk cluster loading weights.

(DLS) results). And since the size of Cu_xS nanodisk cluster is smaller than half wavelength of resonance, and its dielectric functions are similar to $Cu_{27}S_{24}$ [25], we approximated these aggregated nanoclusters into solid spherical $Cu_{27}S_{24}$ nanoparticles of similar size for photothermal study.

Both simulation (Figs. 4(c) and 4(d)) and experimental measured results (Figs. 4(e) and 4(f)) show that solid $Cu_{27}S_{24}$ nanosphere/PVDF nanofilm showed much weaker photothermal response than hollow $Cu_{27}S_{24}$ nanocage/PVDF nanofilm. We attributed this difference to the stronger photothermal response of hollow $Cu_{27}S_{24}$ nanocage. As shown in Fig. 4(b), although the spectrum of hollow $Cu_{27}S_{24}$ nanocage shows slightly weaker intensity to that of solid $Cu_{27}S_{24}$ nanosphere, its mass is less than half (48.8%) of solid $Cu_{27}S_{24}$ nanosphere. Therefore, with same loading weight percentage in the film, hollow $Cu_{27}S_{24}$ nanocage will show higher photothermal conversion efficiency than solid $Cu_{27}S_{24}$ nanosphere, which will lead to the better photothermal performance of the nanofilm.

For completeness, we studied the photothermal performance of $Cu_{27}S_{24}$ nanocages with different shell thickness. Shown in Fig. 5(a), we adjusted the amount of polyvinyl pyrrolidone (PVP) ligands during the synthesis to control the shell thickness while maintaining the diameter of inner cavity (see Methods and Table S3 in the ESM for experimental details). And the 3 types of $Cu_{27}S_{24}$

nanocages with shell thickness of 20, 35, and 45 nm are synthesized and identified by TEM, respectively (images are shown in Figs. 5(b)–5(d). The optical properties of these $Cu_{27}S_{24}$ nanocages are then calculated and shown in Fig. 5(e). The calculated spectrum shows blue-shifted resonance peaks around ~ 1,500 nm and higher intensities as the $Cu_{27}S_{24}$ nanocage shell thickness increases.

These synthesized $Cu_{27}S_{24}$ nanocages were developed into $Cu_{27}S_{24}$ nanocage/PVDF nanofilm, and the experimental measured solar photothermal performances were shown in Figs. S9(a)–S9(c) in the ESM, and their equilibrium temperatures are summarized in Fig. 5(f). All three series of $Cu_{27}S_{24}$ nanocage/PVDF show similar solar photothermal response, and reached plateau of ~ 37 °C. Figures S9(d)–S9(f) in the ESM show their simulated photothermal performance, and their equilibrium temperatures are summarized in Fig. 5(g). $Cu_{27}S_{24}$ nanocage with shell thickness of 20 nm outperformed others, and reached higher temperature after 15 min solar irradiance. We attributed this deviation between simulated model and experiment to the overestimation of simulated threshold temperature of nanofilm. Since the setting of boundary condition in our simulation model is ideal perfect matching layer, which differs from the heat accumulation in the actual experiment, and leads to the lower threshold temperature of these nanofilms in the experiment. The
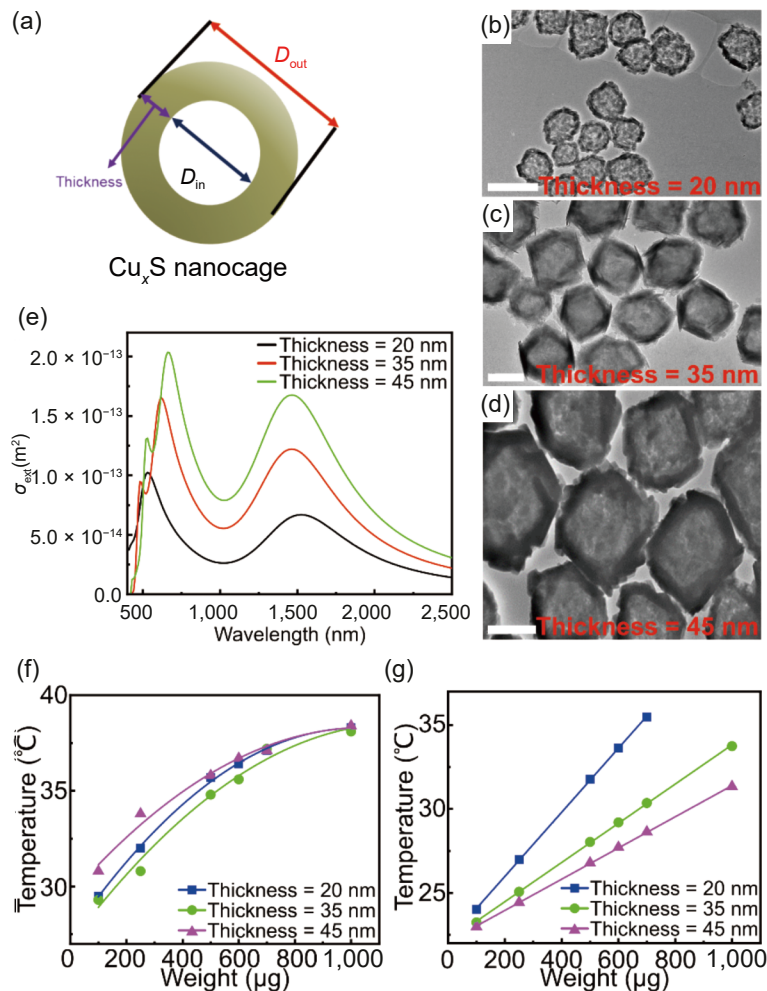
Figure 5 (a) Scheme show hollow $Cu_{27}S_{24}$ nanocage; (b)–(d) TEM images of $Cu_{27}S_{24}$ nanocages with shell thickness of 20, 35, and 45 nm (scale bar = 200 nm); (e) simulated extinction cross section of $Cu_{27}S_{24}$ nanocage with different shell thickness; (f) and (g) experimental measured and simulated equilibrium temperature of $Cu_{27}S_{24}$ nanocage/PVDF nanofilm with different shell thickness and loading weights.

heat transfer coefficients of the simulated environment may also contribute to this deviation.

3 Conclusion

In this paper, hollow colloidal $Cu_{27}S_{24}$ nanocages in covellite crystallinity was synthesized and then processed into "nanoink" and "nanofilm" with excellent solar photothermal response. We used theoretical approach to calculate the optical properties of $Cu_{27}S_{24}$ nanocage by combining first-principle calculations and electromagnetic numerical simulations. The obtained dielectric functions were then used to calculate its photothermal response. In consistent to solar photothermal measurement results, $Cu_{27}S_{24}$ nanocage/PVDF nanofilm showed excellent light-to-heat efficiency. Compare to solid $Cu_{27}S_{24}$ nanospheres, hollow $Cu_{27}S_{24}$ nanocages outperform in solar photothermal conversion efficiency. $Cu_{27}S_{24}$ nanocages with different thickness were also synthesized, and their solar photothermal performances were also evaluated. Our work showed that hollow $Cu_{27}S_{24}$ nanocage has great potential for a large area of solar photothermal applications, such as photothermal imaging, photothermal disinfection, solar steam generation, etc.

4 Methods

4.1 Chemicals and materials

$Cu(NO_3)_2 \cdot 3H_2O$ (AR), PVP (K30, M_W = 40,000 g/mol), hydrazine hydrate (AR, 80%) were purchased from sinopharm chemical

reagent Co., Ltd., NaOH (AR, 96%), $(NH_4)_2S$ aqueous solution (14 wt.%), isopropanol (HPLC ≥ 99.9%) were purchased from Shanghai Macklin. N,N-dimethylformamide (DMF, AR, 96%), PVDF (M_W = 1,000,000 g/mol) were purchased from Shanghai Aladdin biochemical technology Co., Ltd., and deionized water was made in the laboratory. All the reagents were of AR grade, and were used without further purification. Ultrapure water (18.2 MΩ·cm) was produced by a Millipore water purification system.

4.2 $Cu_{27}S_{24}$ nanocage synthesis

The $Cu_{27}S_{24}$ nanocages were synthesized according to the literature with some modifications [37]. Firstly, $Cu(NO_3)_2 \cdot 3H_2O$ (0.01 mol) was dissolved in 50 mL isopropanol at room temperature, followed by dissolving 0.24 g PVP (K30, M_W = 40,000 g/mol) under stirring. Then the pH was adjusted to ~ 9 by adding 10 mL NaOH (0.1 mol/L). After 10 min, 100 μL hydrazine hydrate was added, and the solution was kept stirring for another 10 min (Cu_2O was obtained). After that, 100 μL NH_4S (14 wt.%) aqueous solution was added, and the solution was kept stirring for another hour. The product was washed three times by re-dispersing in ethanol and distilled water mixed solution and centrifuging at 1,000 rpm for 10 min, and then being placed in a vacuum oven to dry completely.

For $Cu_{27}S_{24}$ nanocages with different shell thickness, the thickness of the shell can be adjusted by varying different amount of PVP (experimental conditions are shown in Table S3 in the ESM).

4.3 Cu$_x$S nanodisk synthesis

In a typical synthesis, sulfur powder (0.064 g, 1 mmol) was placed in a 10 mL glass beaker, and then 4 mL oleylamine was added, the color of solution was changed to orange-red after ultra-sonication. CuCl$_2$·2H$_2$O (0.1 g, 1 mmol), 10 mL octadecene and 6 mL oleylamine were then added into a 100 mL three-necked flask, and the solution was stirred and heated to 130 °C under nitrogen and was kept for 30 min. The solution color gradually changed from green to transparent light yellow. Then 4 mL of sulfur precursor was quickly injected into the solution, and the temperature was increased to 180 °C, and was kept for 30 min to promote crystal growth. After the crystal growth, the solution was cooled to room temperature, the dark green Cu$_x$S particles were obtained after being washed by the mixed solution of ethanol and cyclohexane for 3 times, and finally were dispersed in the cyclohexane solution.

The Cu$_x$S nanodisk clusters were developed by dropping 0.5 mL ethanol solution into 5 mL Cu$_x$S nanodisk cyclohexane solution during the magnetic stirring. Then the agglomerated nanoclusters were collected by slow centrifugation speed of ~ 1,500 rpm, and dispersed in ~ 1 mL solution of mixed ethanol and cyclohexane at volume ratio of 1:10 as concentrated solution.

4.4 Cu$_x$S/PVDF nanofilms synthesis

Typically, the Cu$_x$S/PVDF nanofilm was fabricated via evaporating the mixture of colloidal Cu$_{27}$S$_{24}$ nanocages (or Cu$_x$S nanodisk clusters) dispersed in PVDF and DMF solution.

PVDF/DMF solution was first prepared by dissolving 3 g PVDF powder and 30 g N,N-dimethylformamide in a 100 mL beaker with magnetically stirring. Then Cu$_x$S/DMF solution was prepared by dispersing 5 mg Cu$_{27}$S$_{24}$ nanocages powder (or Cu$_x$S nanodisk clusters concentrated solution) in 500 μL DMF during ultrasonication.

And the Cu$_x$S/PVDF precursor was prepared as follows: 1 g of the previously prepared PVDF/DMF solution and different amount of Cu$_x$S/DMF solution (10, 25, 50, 60, 70, and 100 μL) were mixed, and then was placed in a glass petri dish (diameter = ~ 2 cm). Then the precursor bulk sample was placed in a vacuum oven to remove excessive bubbles, and finally was dried in a 60 °C oven for 4 h. Then the formed nanofilm was gently peeled off from the petri dish as the resulting product.

4.5 TEM imaging

The nanostructures characterization was performed by TEM(JEM-2100F, JEOL) with the accelerating voltage of 160 kV to study the microscopic morphology, crystal structure, and phase structure of samples. And the morphological characterization was performed by using an image software "Nano Measure" (Jie Xu, Fudan University, shine6832@163.com) to process the TEM images. And the size distributions of the sample (diameters and thickness) are summarized in Fig. S1 in the ESM.

4.6 SEM imaging, EDS and XPS analysis

The morphology of nanoparticles characterization was performed with a field emission scanning electron microscope. The surface morphology was obtained by FESEM (SU8020, HITACHI) with the acceleration voltage of 10 kV. High-resolution scanning and EDS were obtained by a focused ion beam scanning electron microscope (FIB-SEM Zeiss) attached with an EDS machine (energy dispersive spectroscopy, Oxford link and ISIS 300). XPS analysis was performed on ESCALAB 250Xi (thermo-scientific).

4.7 XRD measurement

The XRD was obtained on powder X-ray diffraction (X'Pert-Pro MPD, PANalytical) using an X-ray diffractometer with Cu Kα radiation (λ = 1.5418 Å). Scans were collected on dry sample powder in the range of 2θ = 10°–80°. The obtained characterization raw results are processed with standard Rietveld refinement with fullpro and autoFP software to correct the baseline and background noises.

4.8 FTIR measurement

The Fourier transform infrared measurement of Cu$_{27}$S$_{24}$ nanocage was performed by iS50R FT-IR (thermo scientific) with beam splitter of KBr tablet, the scans are collected and averaged into the resulting spectrum.

4.9 Optical measurement

The optical responses of Cu$_{27}$S$_{24}$ nanocages were characterized by UV–vis–NIR spectrometer UV-3600 (SHIMADZU) and MPC 3100 (SHIMADZU) equipped with integrating sphere. The sample spectrum was recorded at wavelength range of 400–2,500 nm and slit width of 2 nm in liquid phase (CCl$_4$ as the solvent). And the recorded spectra was normalized and fitted by the Gaussian peak to determine the resonance peak and FWHM.

4.10 Cu$_x$S nanoink for "photothermal visible calligraphy"

Typically, 10 mg Cu$_{27}$S$_{24}$ nanocages were dispersed into 10 mL ethanol after vigorous ultrasonication (KQ-400KDB, 100 kHz, 400 W) for 5 min. Then, the freshly prepared colloidal solution was directly used as the "ink" for "photothermal visible calligraphy" with a common writing brush and a paper of dark color.

4.11 Photothermal test

The phtothermal test was performed at an ambient temperature of 22 °C. The nanofilm samples were placed on foam board (for thermal isolation), and then were irradiated by a solar simulator with illumination intensity of ~ 1,000 W/m^2. The sample was recorded with thermalgraphic camera to obtain the infrared image and temperature distribution.

4.12 Cu$_{27}$S$_{24}$ optical constant calculations

We determined the dielectric functions of Cu$_{27}$S$_{24}$ via a combination of density functional theory (DFT) calculation and electromagnetic simulation using.

The first principle calculation was performed by materials studio as a commercial software. The lattice parameters (such as lengths, atom positions, angles, etc.) adopted from literature reference of covellite CuS were used to create Cu$_{27}$S$_{24}$ supercell [33]. Then geometry optimization and optical properties calculations were performed with CASTEP module. The calculated atoms coordinates are summarized in Table S1 in the ESM. Then the damping constant γ = 0.44 eV and different values of bulk plasma frequency ω_p were used to estimate the dielectric function according to the literature reference (Fig. S6(a) in the ESM).

Since the Mie theory can only be applied to spherical shaped nanoparticle, we performed numerical simulations with each derived dielectric function of Cu$_{27}$S$_{24}$ to select the most accurate dielectric function of Cu$_{27}$S$_{24}$. The structures were designed using in commercial FEM software (COMSOL multiphysics). The simulation of extinction cross section of single nanoparticle was performed in the module of wave optics. Shown in Fig. S6(b) in the ESM, Cu$_{27}$S$_{24}$ nanocage were described as a spherical shell with diameter of 150 nm and shell thickness of 20 nm based on the TEM characterization of the synthesized nanostructures, the structures were surrounded by a sphere representing the surrounding medium of organic solvent, and enclosed by a perfect

matching layer, which prevented unwanted reflections from the outside boundary. A plane wave polarized in X direction was set to excite the resonance of the particle with the Poynting's vector in Z direction. The derived dielectric function of $Cu_{27}S_{24}$ and CCl_4 medium ($\varepsilon_m = 2.25$) were applied to each domain. After solving the partial differential equation, the extinction cross section of the particle was then evaluated by integrating over the particle.

The simulated spectrum of $Cu_{27}S_{24}$ nanocages with dielectric functions derived from different bulk plasma frequencies (ω_p) are shown in Fig. S6(c) in the ESM. The LSPR peaks of these calculated spectrum can be extrapolated by Gaussian fit, and show linear relationship to the bulk plasma frequencies (ω_p): $\omega_{LSPR} = 0.1535\omega_p + 0.1489$. According to the experimental measured UV–vis-NIR spectrum, $Cu_{27}S_{24}$ nanocage shows $\omega_{LSPR} = 0.81$ eV, and the bulk plasma frequencies of the synthesized $Cu_{27}S_{24}$ material can be calculated from the empirical equation mentioned above as $\omega_p = 4.31$ eV, which can be used to derive the resulting dielectric function of $Cu_{27}S_{24}$ (indicated in Fig. 2(c)).

4.13 Solar photothermal simulations

The heat transfer module of COMSOL multiphysics was used to calculate photothermal response. As shown in Fig. S7 in the ESM, the test sample film (indicated in blue meshes) was modeled as cylinder with height = 0.05 cm, and diameter = 2.0 cm in the space of air. The input radiance was set perpendicular to the sample film at Z direction.

The partial differential equations Eqs. (1) and (2) were solved to calculate the temperature distribution of the system. Equation (1) describes the thermal equilibrium of the overall system, where Q_r is the generated heat; ρ_{air}, ρ_{film} and C_{air}, C_{film} are the density and heat capacity of air and film, respectively.

$$\frac{\partial Q_r}{\partial t} = \rho_{air} C_{air} \frac{\partial T_{air}}{\partial t} + \rho_{film} C_{film} \frac{\partial T_{film}}{\partial t} \qquad (1)$$

Equation (2) describes the photothermal process, where K_{film} is the absorption coefficient of film, G is the radiation power density.

$$\frac{\partial Q_r}{\partial t} = K_{film} G \qquad (2)$$

Since the solar intensive band covers the light wavelength from 400 to 2,500 nm, for the convenience of FEM methods calculation, we approximates the solar spectrum into a series of elemental beams. As shown in Fig. S10 in the ESM, the original solar spectrum (blue curve) was first smoothed with polynomial fit (red curve), and then processed into a series of elemental beams (green curve).

$$I_i = \frac{I_0}{\sqrt{2\pi}\sigma} e^{-\frac{(f-f_0)^2}{2\sigma^2}} \qquad (3)$$

Each elemental beam is described by the Gaussian fit curve (Eq. (3)), where I_i is each processed intensity of beam, I_0 is the corresponding intensity of smoothed solar spectrum, f_0 is the central frequency of the beam, and σ is the standard deviation that proportional to D_i (beam diameter of $1/e^2$ width) defined as $\sigma = \frac{D_i}{f_0}$.

Shown in Eq. (4), G is the incident solar radiation intensity, a_i is each approximated portion of elemental Gaussian beam of overall solar irradiance power, I_i is the corresponding intensity of elemental beam to each frequency.

$$G = \sum a_i \cdot I_i \qquad (4)$$

Described as Eq. (5), the absorption coefficient of film is

described as the sum of α_i, which is the absorption coefficient at each frequency. α_i can be calculated from Eq. (6), where σ_{CuS} is the calculated extinction cross section of wave optics module of Cu_xS nanoparticles, and n_{CuS} is the total amount of Cu_xS nanoparticles in the film.

$$K_{film} = \sum \alpha_i \qquad (5)$$

$$\alpha_i = \sigma_{CuS} \cdot n_{CuS} \qquad (6)$$

Therefore, the partial differential equation to be solved can be written as Eq. (7).

$$\frac{\partial Q_r}{\partial t} = \sum \alpha_i \cdot a_i \cdot I_i = \rho_{air} C_{air} \frac{\partial T_{air}}{\partial t} + \rho_{film} C_{film} \frac{\partial T_{film}}{\partial t} \qquad (7)$$

The simulated results are summarized in Fig. S10(i) in the ESM. Different value of σ are applied to the model to express light source of solar irradiance. The average temperature of Cu_xS/PVDF film increased as the solar irradiation time. After ~ 6 min illumination, the temperature of the film reached a plateau of equilibrium. And the temperature at equilibrium decreases as the standard deviation σ of elemental beam, though the equilibrium temperature almost the same for $\sigma < 0.02$. Since σ of monochromatic laser beam is usually larger than 0.02, we choose $\sigma = 0.02$ for calculation.

Acknowledgements

Electronic Supplementary Material: Supplementary material (EDS analysis results, XRD pattern, modeled $Cu_{27}S_{24}$ supercell atoms coordinates, XPS spectrum, FTIR spectrum, DLS) measurement results and other information) is available in the online version of this article at https://doi.org/10.1007/s12274-021-3880-3.

References

[1] Zhang, Y. C.; He, S.; Guo, W. X.; Hu, Y.; Huang, J. W.; Mulcahy, J. R.; Wei, W. D. Surface-plasmon-driven hot electron photochemistry. *Chem. Rev.* **2018**, *118*, 2927–2954.

[2] Tang, H. B.; Chen, C. J.; Huang, Z. L.; Bright, J.; Meng, G. W.; Liu, R. S.; Wu, N. Q. Plasmonic hot electrons for sensing, photodetection, and solar energy applications: A perspective. *J. Chem. Phys.* **2020**, *152*, 220901.

[3] Li, J.; Wong, W. Y.; Tao, X. M. Recent advances in soft functional materials: Preparation, functions and applications. *Nanoscale* **2020**, *12*, 1281–1306.

[4] Jiang, N. N.; Zhuo, X. L.; Wang, J. F. Active plasmonics: Principles, structures, and applications. *Chem. Rev.* **2018**, *118*, 3054–3099.

[5] Sun, Y. H.; Jiang, L.; Zhong, L. B.; Jiang, Y. Y.; Chen, X. D. Towards active plasmonic response devices. *Nano Res.* **2015**, *8*, 406–417.

[6] Eustis, S.; El-Sayed, M. A. Why gold nanoparticles are more

precious than pretty gold: Noble metal surface plasmon resonance and its enhancement of the radiative and nonradiative properties of nanocrystals of different shapes. *Chem. Soc. Rev.* **2006**, *35*, 209–217.

[7] Zhao, L. Y.; Shang, Q. Y.; Li, M. L.; Liang, Y.; Li, C.; Zhang, Q. Strong exciton-photon interaction and lasing of two-dimensional transition metal dichalcogenide semiconductors. *Nano Res.* **2021**, *14*, 1937–1954.

[8] Zhang, C. Y.; Jia, F. C.; Li, Z. Y.; Huang, X.; Lu, G. Plasmon-generated hot holes for chemical reactions. *Nano Res.* **2020**, *13*, 3183–3197.

[9] Naik, G. V.; Shalaev, V. M.; Boltasseva, A. Alternative plasmonic materials: Beyond gold and silver. *Adv. Mater.* **2013**, *25*, 3264–3294.

[10] West, P.; Ishii, S.; Naik, G. V.; Emani, N. K.; Shalaev, V. M.; Boltasseva, A. Searching for better plasmonic materials. *Laser Photonics Rev.* **2010**, *4*, 795–808.

[11] Tang, X.; Ackerman, M. M.; Guyot-Sionnest, P. Thermal imaging with plasmon resonance enhanced HgTe colloidal quantum dot photovoltaic devices. *ACS Nano* **2018**, *12*, 7362–7370.

[12] Wu, J. B.; Wang, N.; Yan, X. D.; Wang, H. Emerging low-dimensional materials for mid-infrared detection. *Nano Res.* **2021**, *14*, 1863–1877.

[13] Agrawal, A.; Johns, R. W.; Milliron, D. J. Control of localized surface plasmon resonances in metal oxide nanocrystals. *Annu. Rev. Mater. Res.* **2017**, *47*, 1–31.

[14] Xi, M.; Reinhard, B. M. Localized surface plasmon coupling between mid-IR-resonant ITO nanocrystals. *J. Phys. Chem. C* **2018**, *122*, 5698–5704.

[15] Kuznetsov, A. S. Effect of proximity in arrays of plasmonic nanoantennas on hot spots density: Degenerate semiconductors vs. conventional metals. *Plasmonics* **2016**, *11*, 1487–1493.

[16] Liu, B.; Ma, Y. R.; Zhao, D. Y.; Xu, L. H.; Liu, F. S.; Zhou, W.; Guo, L. Effects of morphology and concentration of CuS nanoparticles on alignment and electro-optic properties of nematic liquid crystal. *Nano Res.* **2017**, *10*, 618–625.

[17] Abb, M.; Wang, Y. D.; Papasimakis, N.; de Groot, C. H.; Muskens, O. L. Surface-enhanced infrared spectroscopy using metal oxide plasmonic antenna arrays. *Nano Lett.* **2014**, *14*, 346–352.

[18] Luther, J. M.; Jain, P. K.; Ewers, T.; Alivisatos, A. P. Localized surface plasmon resonances arising from free carriers in doped quantum dots. *Nat. Mater.* **2011**, *10*, 361–366.

[19] Xu, Q.; Huang, B.; Zhao, Y. F.; Yan, Y. F.; Noufi, R.; Wei, S. H. Crystal and electronic structures of Cu_xS solar cell absorbers. *Appl. Phys. Lett.* **2012**, *100*, 061906.

[20] Azzam, S. A.; Boubnov, A.; Hoffman, A. S.; López-Ausens, T.; Chiang, N.; Canning, G.; Sautet, P.; Bare, S. R.; Simonetti, D. A. Insights into copper sulfide formation from Cu and S K edge XAS and DFT studies. *Inorg. Chem.* **2020**, *59*, 15276–15288.

[21] Huang, S.; Liu, J.; He, Q.; Chen, H. L.; Cui, J. B.; Xu, S. Y.; Zhao, Y. L.; Chen, C. Y.; Wang, L. Y. Smart $Cu_{1.75}S$ nanocapsules with high and stable photothermal efficiency for NIR photo-triggered drug release. *Nano Res.* **2015**, *8*, 4038–4047.

[22] Zou, X. X.; Zhang, Y. Noble metal-free hydrogen evolution catalysts for water splitting. *Chem. Soc. Rev.* **2015**, *44*, 5148–5180.

[23] He, C. H.; Duan, D. L.; Low, J.; Bai, Y.; Jiang, Y. W.; Wang, X. Y.;

Chen, S. M.; Long, R.; Song, L.; Xiong, Y. J. $Cu_{2-x}S$ derived copper nanoparticles: A platform for unraveling the role of surface reconstruction in efficient electrocatalytic CO_2-to-C_2H_4 conversion. *Nano Res.*, in press, DOI: 10.1007/s12274-021-3532-7.

[24] Raj, S. I.; Jaiswal, A.; Uddin, I. Ultrasmall aqueous starch-capped CuS quantum dots with tunable localized surface plasmon resonance and composition for the selective and sensitive detection of mercury(II) ions. *RSC Adv.* **2020**, *10*, 14050–14059.

[25] Zhang, N. W.; Wang, C.; Liu, W. D.; Lei, X. F.; Zhao, J.; Huang, H.; Zhang, X. H.; Hu, Y. M.; Li, Y. B. Contronable synthesis and optical properties of semiconductor CuS nanoplates. *J. Hubei Univ. (Nat. Sci.)* **2020**, *42*, 61–66, 71.

[26] Shao, X.; Zhang, T. Y.; Li, B.; Wu, Y.; Ma, X. Y.; Wang, J. C.; Jiang, S. Cu-deficient plasmonic $Cu_{2-x}S$ nanocrystals induced tunable photocatalytic activities. *CrystEngComm* **2020**, *22*, 678–685.

[27] Jiang, L. S.; Wang, K.; Wu, X. Y.; Zhang, G. K. Highly enhanced full solar spectrum-driven photocatalytic CO_2 reduction performance in $Cu_{2-x}S/g$-C_3N_4 composite: Efficient charge transfer and mechanism insight. *Sol. RRL* **2021**, *5*, 2000326.

[28] Prodan, E.; Radloff, C.; Halas, N. J.; Nordlander, P. A hybridization model for the plasmon response of complex nanostructures. *Science* **2003**, *302*, 419–422.

[29] Gómez, D. E.; Teo, Z. Q.; Altissimo, M.; Davis, T. J.; Earl, S.; Roberts, A. The dark side of plasmonics. *Nano Lett.* **2013**, *13*, 3722–3728.

[30] Zhou, H. P.; Pan, Z. Z.; Dedo, M. I.; Guo, Z. Y. High-efficiency and high-precision identification of transmitting orbital angular momentum modes in atmospheric turbulence based on an improved convolutional neural network. *J. Opt.* **2021**, *23*, 065701.

[31] Amendola, V.; Pilot, R.; Frasconi, M.; Maragò, O. M.; Iatì, M. A. Surface plasmon resonance in gold nanoparticles: A review. *J. Phys.: Condens. Matter* **2017**, *29*, 203002.

[32] Jaque, D.; Maestro, L. M.; del Rosal, B.; Haro-Gonzalez, P.; Benayas, A.; Plaza, J. L.; Rodríguez, E. M.; Solé, J. G. Nanoparticles for photothermal therapies. *Nanoscale* **2014**, *6*, 9494–9530.

[33] Takéuchi, Y.; Kudoh, Y.; Sato, G. The crystal structure of covellite CuS under high pressure up to 33 *kbar*. *Z. Krist.* **1985**, *173*, 119–128.

[34] Qu, Y. N.; Xu, X. J.; Huang, R. L.; Qi, W.; Su, R. X.; He, Z. M. Enhanced photocatalytic degradation of antibiotics in water over functionalized N, S-doped carbon quantum dots embedded ZnO nanoflowers under sunlight irradiation. *Chem. Eng. J.* **2020**, *382*, 123016.

[35] Nie, G. D.; Zhang, L.; Lu, X. F.; Bian, X. J.; Sun, W. N.; Wang, C. A one-pot and *in situ* synthesis of CuS-graphene nanosheet composites with enhanced peroxidase-like catalytic activity. *Dalton Trans.* **2013**, *42*, 14006–14013.

[36] Pang, X. C.; He, Y. J.; Jung, J. H.; Lin, Z. Q. 1D nanocrystals with precisely controlled dimensions, compositions, and architectures. *Science* **2016**, *353*, 1268–1272.

[37] Pang, M. L.; Zeng, H. C. Highly ordered self-assemblies of submicrometer Cu_2O spheres and their hollow chalcogenide derivatives. *Langmuir* **2010**, *26*, 5963–5970.